Spin Dynamics of Low Phosphorus-doped Silicon in the Low-Temperature and High-Field Limits

研究報告１１

Spin Dynamics of Low Phosphorus-doped Silicon in the Low-Temperature and High-Field Limits

Takao Mizusaki[1,2,3], Myeonghun Song[4], Minki Jeong[4], Byeongki Kang[4], Soonchil Lee[4], Tomohiro Ueno[5], Akira Matsubara[6], Yutaka Fujii[3], Seitaro Mitsudo[3], and Meiro Chiba[7,8]

[1] *Physics Department, Graduate School of Science, Kyoto University, 606-8502, Japan*

[2] *Toyota Physical and Chemical Research Institute, Nagakute, Aichi 480-1192, Japan*

[3] *Research Center for Development of Far-Infrared Region, University of Fukui, Fukui 910-8507, Japan*

[4] *Department of physics, KAIST, Daejeon 305-701, Republic of Korea*

[5] *Graduate School of Medicine, Kyoto University, Kyoto 606-8501, Japan*

[6] *Research Center for Low Temperature and Materials Sciences, Kyoto University, 606-8501, Japan*

[7] *Graduate School of Engineering, University of Fukui, Fukui 910-8507, Japan*

[8] *Research Center for Quantum Computing, Interdisciplinary Graduate School of Science and Technology, Kinki University, Higashi-Osaka 577-8502, Japan*

Abstract

Spin dynamics of shallow-trapped donor electron spins in Si:P (phosphorous-doped silicon) has been studied by high frequency ESR. A sample with the donor concentration 6.5 x 10^{16} cm^{-3}, where the sample is a insulator at low temperatures and the donor is almost isolated, was investigated at 2.87 T (80 GHz) from 48 K to 1.8 K by cw-ESR with field modulation. At low temperatures, where the spin-lattice relaxation time T_1 changes in many orders of magnitude, the resonance line shape changed from the usual derivative form of the absorption line at high temperatures to the non-derivative shape caused by the passage effects at low temperatures. These complex behaviors in the resonance line shape have made it possible to estimate the spin-lattice relaxation time T_1. We numerically solved the Bloch equations for a given inhomogeneous line shape and obtained the ESR absorption and dispersion signal as a function of the spin lattice relaxation time T_1. We analytically solve Bloch equations at the low-temperature limit ($\varepsilon_F >> 1$) to understand spin dynamics. The observed T_1 at a high field of 2.87 T is consistent with the reported T_1 for samples with the low dopant concentration limit at 0.32 ~ 0.33 T after the theoretical correction for the magnetic field dependence. Possible dynamic nuclear polarization effect on ^{31}P nuclear spin was observed in asymmetry of ESR intensities between two hyperfine states.

I. Introduction

One of the most thoroughly studied quantum systems for a quantum computer is the silicon-based solid state quantum computer model proposed by Kane [1]. The model uses the phosphorus (P) nuclear spins embedded regularly in silicon crystal as Q-bits, where for quantum computer operations, electron spins should be completely polarized by high fields (several Tesla) and low temperatures in the range of 100 mK. We report here ESR results[4, 5] of insulator samples with P-concentration $n = 6.5 \times 10^{16}$ cm^{-3}, where doped P in Si crystal are isolated impurities. As for the basic natures of Si:P, many studies have been reported from 1950 to 1970. The ESR of the donor electron spin has been performed [6, 18], focusing on the metal-insulator transition with varying P-donor concentrations, where the critical P-concentration is $n_c = 3.7 \times 10^{18}$ cm^{-3}[19]. We performed ESR at high field of several Tesla and focused on 1) electron-spin longitudinal relaxation times T_1 (T) in order to check the possibility that electron spin-temperature could be cooled down to 100 mK-temperature range under high fields and 2) the dynamic P-nuclear polarization (DNP) by pumping electron spin by ESR, which is important for one of the possible ways to set up a initial condition of each Q-bit. NMR for low-concentration Si:P sample (insulator), which has not been observed, may become possible by using the DNP. 3) Long time coherence of a Q-bit, which is necessary for the quantum computation, could not be studied in this sample, since T_2 of the isolated ^{31}P nuclear is determined by ^{31}P-^{29}Si dipole interaction unless 4 % of natural abundant ^{29}Si with nuclear spin $I = 1/2$ is eliminated from Si sample. The T_2 of ^{31}P nuclear spin in Si:P with natural abundant ^{29}Si should be expected to be about 20 ms [2, 3].

2. Experimental Set-up and Results

The high frequency ESR was measured at 80 GHz from 48 K down to 1.8 K under the magnetic field of about 2.87 T applied by a superconducting magnet. The microwave source was a Gunn oscillator which was operated by the phase-locked mode with the Millimeter-Wave Vector Network Analyzer (MVNA:ABmm). The block diagram of the experimental setup is shown in Fig. 1. The sample of Si:P with the donor concentration 6.5 x 10^{16} cm^{-3} was set in the circular waveguide. The size of the sample was 3 x 3 x 0.3 mm^3. In order to observe the absorption signal a simple transmission method was adopted without cavity resonator. By the transmission method we expected to avoid the mixing of the dispersion signal into the absorption signal, but the actual microwave transmission was found to be not simple. Because of unexpected mismatching of the impedance, observed ESR signals was not pure absorption but slight mixtures with dispersion signal in the waveguide. The microwave signal was detected by an InSb hot electron low-noise detector operated at 4.2 K. The ESR signal was observed with the external field modulation of frequencies $\omega_m / 2\pi = 330$ and 590 Hz [5] and 15 kHz [4] by the lock-in detection of the signal from the hot electron detector.

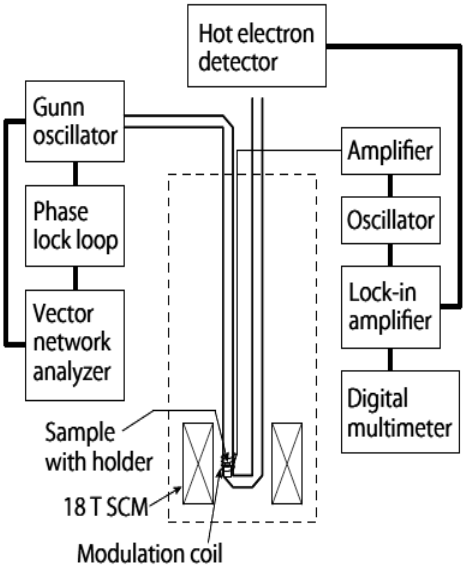

Fig. 1. Block diagram of the mm-wave ESR system (20-200 GHz)

Typical ESR spectra of Si:P at $\omega_m / 2\pi = 330$ Hz and a modulation-field strength $B_m = 9.1 \times 10^{-5}$ T are summarized at various temperatures in Fig. 2. The audio-frequency phase for the field modulation was adjusted in such a way that the 90◦ out-of-phase signal (hereafter referred as the

out-of-phase signal) was zero and only the in-phase signal appeared for $T > 16$ K, which is the temperature region for the slow passage condition. In-phase signals are shown in Fig. 2 (a) and the out-of-phase in Fig. 2 (b). Below about 30 K, ESR lines of the isolated donor electrons were split into two lines (denoted by higher-field line (H-line) and lower-field line (L-line)) separated by 4.2 mT by hyperfine interaction. These two lines are merged into one line above 40 K by the motional narrowing of thermal electron's hopping motion between donor sites [20]. We focus to signals below 20 K, which come from isolated electron spins trapped at P-donor site.

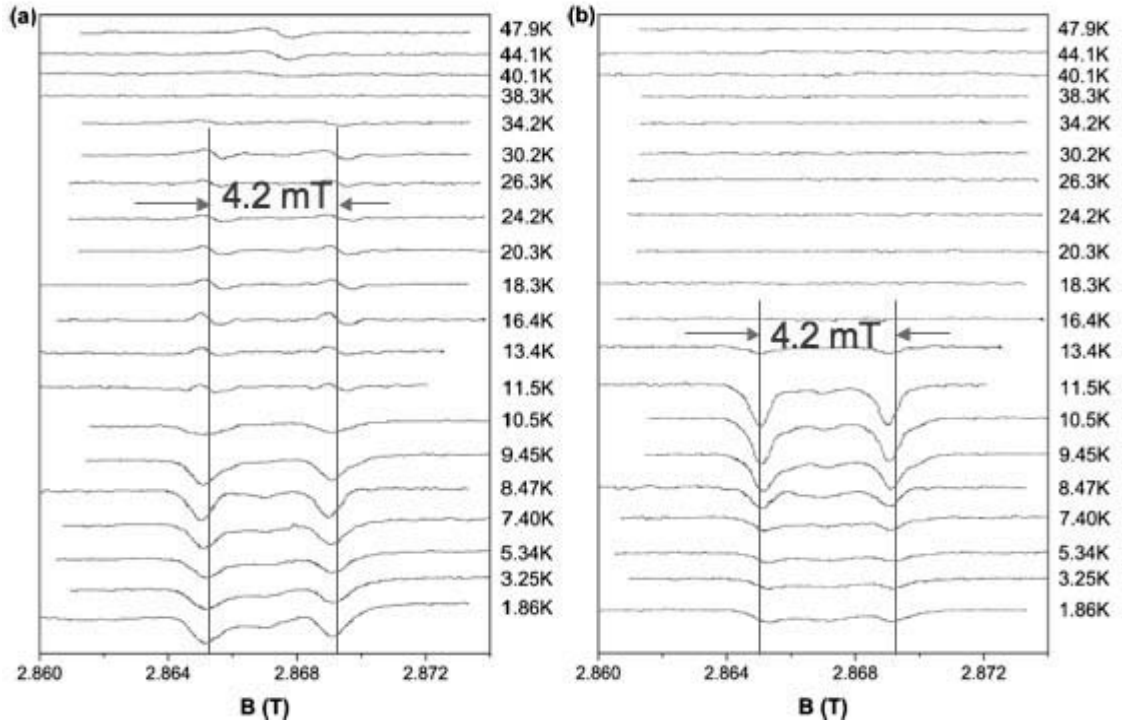

Fig. 2. Typical ESR spectra for in-phase (a) and out-of-phase (b) at various temperatures and 80 GHz.

Below 20 K, there are three temperature regions, I (1.5 K < T < 11.5 K), II (11.5 K < T < 16 K) and III (16 K < T < 20 K) according to shapes of the ESR spectra and appearance of the out-of-phase signals. In the region III, the line shape of the in-phase signal was the odd function in $\delta\omega$, which is the derivative of the absorption line shape and usually is observed in the ESR experiment with the field modulation method under the slow passage condition, where $\delta\omega = \omega - \omega_a$ and ω_a is one of the hyperfine resonance frequencies. There is no out-of-phase signal. While in the region I both the in-phase and out-of-phase line-shapes were even function in $\delta\omega$, which are no more the derivative of the

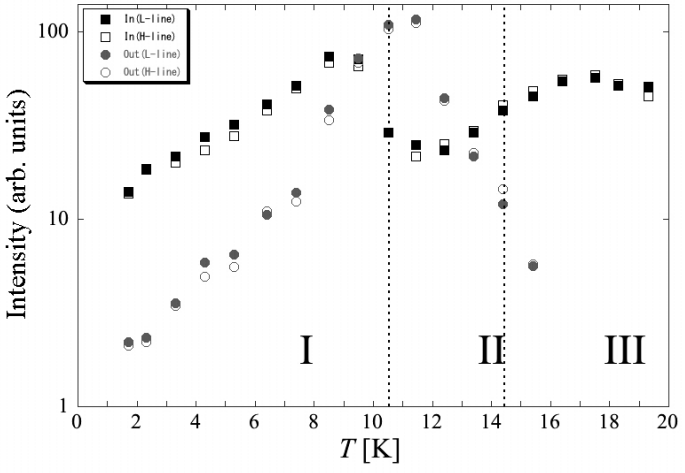

Fig. 3 Temperature dependence of normalized intensities. Squares are for in-phase and circles are for out-of-phase and solid symbols are for L-lines and open ones for H-lines.

resonance lines. The region II is the transition region where out-of phase signals appear and are purely even functions, on the other hand the in-phase signals are the mixture between even and odd functions. As is well known, the out-of-phase signal is not observed under the slow passage condition and thus the slow passage condition breaks down in the region I and II.

In Fig. 3, the temperature dependence of ESR signal intensities are shown for the in-phase signal (squares) and the out-of-phase signal (circles). The solid symbols are intensities for the L-line and open symbols are for the H-line. The intensities are normalized by the Brillouin function, namely, intensities divided by $\tanh(\mu_B B/2k_B T)$ for S = 1/2 and B = 2.87 T in convenience to compare the intensity with the result of the numerical calculation in Section 3, where Bohr magneton $\mu_B = \hbar\gamma$ and γ= 1.76 x 10^{11} rad/s T is the gyromagnetic ratio of electron spin. Modulation frequency $\omega_m/2\pi$ is 330 Hz. Intensities of the in-phase signal were measured as peak-to-peak values in III and II, and as peak heights in I. Intensities of the out-of-phase signals, which only appear in I and II, were always measured by the peak height. Below 6 K, there are very broad background signals, which are subtracted from ESR intensities for H- and L-lines, respectively.

It is noted that at low temperature below about 10 K the intensities of the L-line shown by solid symbols are always larger by about 10 % than that of the H-line shown by open symbols. We attribute this asymmetry of 10 % between the L- and H-lines to the DNP of ^{31}P-nuclear spin but are ignored in the analysis until the DNP effects on ^{31}P nuclear spins will be discussed in Section 5.

3. Numerical solution for Bloch equations for inhomogeneously-broadened spectrum

We took cw-ESR with the field-modulation method. Since T_1 changes in many orders of magnitude in the temperature range of our measurement [6. 7, 12], the various passage conditions such as the rapid, fast and adiabatic passage change in temperatures. We numerically solve Bloch equations and obtain the lock-in detected in- and out-of-phase signals as a function of T_1. Both H- and L-lines are inhomogeneously broadened by the hyperfine interaction between ^{31}P and randomly-distributed ^{29}Si and the width is temperature-independent. We determined the inhomogeneously-broadened line shape by integrating the in-phase signal at T = 20 K in the region III, shown in Fig. 4. The open circles are data and the solid curve is a fit to the Gaussian function of h (ω, ω_{res}) as,

$$h(\omega,\omega_a)=\frac{1}{\sqrt{2\pi}\sigma}\exp\left(-\frac{(\omega-\omega_a)^2}{2\sigma^2}\right), \quad (1)$$

where ω_a is one of the central frequencies of the H- or L-lines. The fitted value of σ is 6.2 x 10^{7} rad/s, which is similar to reported values[10].

From this spectrum, we pick up a wave packet at ω', which obeys Bloch equations [20] in the rotating frame of $\omega = \gamma B_0$ as follows:

$$\frac{dM_x}{dt} = -\gamma b_z M_y - \frac{M_x}{T_2}$$

$$\frac{dM_y}{dt} = \gamma b_z Mx - \gamma B_1 M_z - \frac{M_y}{T_2}$$

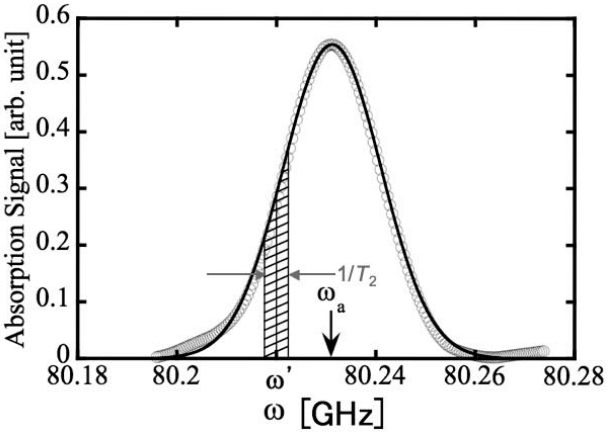

Fig. 4 ESR absorption line shape observed at a high temperature of 17 K in the region III.

$$\frac{dM_z}{dt} = \gamma B_1 M_y - \frac{M_z - M_0}{T_1} \quad . \tag{2}$$

The residual magnetic field b_z along z-axis in the rotating frame ω' is given by,

$$b_z = \frac{\delta\omega}{\gamma} + B_m \cos\omega_m t \,, \tag{3}$$

where $\delta\omega = \omega - \omega' = \gamma B_0 - \omega'$ and B_m and ω_m are the amplitude and the angular frequency of the modulation field. We choose $B_m = 9.1 \times 10^{-5}$ T and $\omega_m/2\pi = 330$ Hz. The microwave power B_1 is not well known and is treated as a fitting parameter. We choose $B_1 = 1.1 \times 10^{-6}$ T in the numerical calculation. The T_2 weekly depend on temperatures [11, 12] and we choose $T_2 = T_1$ (the motional narrowing) when $T_1 < 10^{-4}$ s and $T_2 = 10^{-4}$ s (the rigid lattice, independent of temperatures) when $T_1 > 10^{-4}$ s. Therefore the main temperature dependence of the Bloch solution comes from $T_1(T)$ [6, 7, 12].

The effect of the passage condition on spectral line shape has been discussed in some limiting case, for example by Portis [21] and Weger [22]. Three important parameters, which specify various passage conditions, are defined as,

$$\begin{aligned} \varepsilon_A &= \frac{\gamma {B_1}^2}{B_m \omega_m} \\ \varepsilon_R &= \left(\frac{B_m}{B_1}\right)\omega_m T_1 \\ \varepsilon_F &= \omega_m T_1 \end{aligned} \tag{4}$$

For parameters B_m, ω_m, and B_1 chosen above, the adiabatic fast passage $\varepsilon_A \sim 1$ and the rapid passage $\varepsilon_R \sim 100\ \varepsilon_F$, the relation of which are temperature-independent. The numerical calculations of Bloch equations are carried out to obtain the final results for the lock-in output of the in-phase $V^{IN}(\omega - \omega_a)$ and the out-of-phase $V^{OUT}(\omega - \omega_a)$ by 4 steps.

(1) First, we explicitly solved Bloch equations Eq. (2) for spin packets with ω' by using GNU Scientific Library and obtained time evolutions of $\boldsymbol{M}(t)$ at a given $\delta\omega$ defined by Eq. (3). The value of M_0 is chosen to be 1 so that the obtained intensity should be normalized by Brillouin function for $S = 1/2$.

(2) After steady-state solutions $M_\alpha(t, \delta\omega, T_1)$ were obtained at $t > 5\ T_1$, the time average of the steady-state solutions over the period of the field modulation $2\pi/\omega_m$ were calculated as,

$$\overline{M_\alpha \cos\omega_m t}\,(\delta\omega, T_1) = \frac{\omega_m}{2\pi}\int_0^{2\pi/\omega_m} M_\alpha(t, \delta\omega, T_1)\cos\omega_m t\, dt \,, \tag{5}$$

where $\alpha = x, y$. Similarly we can calculate $\overline{M_\alpha \sin\omega_m t}\,(\delta\omega, T_1)$.

(3) The in- and out-of-phase output signals $M_\alpha^{IN}(\omega - \omega_a)$ are calculated by taking convolution of the response function, Eq. (5), with $h(\omega, \omega_a)$ as,

$$M_\alpha^{IN}(\omega - \omega_a) = \int_{-\infty}^{+\infty} \overline{M_\alpha(\omega' - \omega)\cos\omega_m t}\; h(\omega', \omega_a)\, d\omega' \,, \tag{6}$$

and $M_\alpha^{OUT}(\omega - \omega_a)$ is calculated similarly as Eq. (6), where $\alpha = x, y$.

(4) The in- and out-of-phase output signal, $V^{IN}(\omega\text{-}\omega_a)$ and $V^{OUT}(\omega-\omega_a)$ are calculated by properly mixing M_x with M_y as,

$$V^{IN}(\omega-\omega_a)=M_x^{IN}(\omega-\omega_a)+A\cdot M_y^{IN}(\omega-\omega_a)$$
$$V^{OUT}(\omega-\omega_a)=M_x^{OUT}(\omega-\omega_a) \tag{7}$$

where the parameter A is the mixing parameter between the absorption M_y and the dispersion M_x. This A should be adjusted experimentally but we choose $A = 4$ by adjusting the ratio of the plateau value of V^{IN} in the region III to the peak height of V^{IN} in the region I (see Fig. 6).

Typical solutions for various passage conditions are shown in Fig. 5, where the column I is the case for $T_1 = 10^{-1}$ s and $T_2 = 10^{-4}$ s, the column II for $T_1 = 10^{-4}$ s and $T_2 = 10^{-4}$ s and the column III for $T_1 = T_2 = 10^{-6}$ s. In the region I (the rapid and fast passages) corresponds to $\varepsilon_R >> 1$ and $\varepsilon_F >> 1$, the region II (the rapid and non-fast passages) to $\varepsilon_R >> 1$ and $\varepsilon_F < 1$ and the region III (the slow and non-fast passages) to $\varepsilon_R << 1$ and $\varepsilon_F < 1$. Figure 5 (I-a), (II-a), and (III-a) show the steady-state time evolutions of $\boldsymbol{M}(t)$ at $\delta\omega = 0$ for various passage conditions. Figure 5 (I-b),

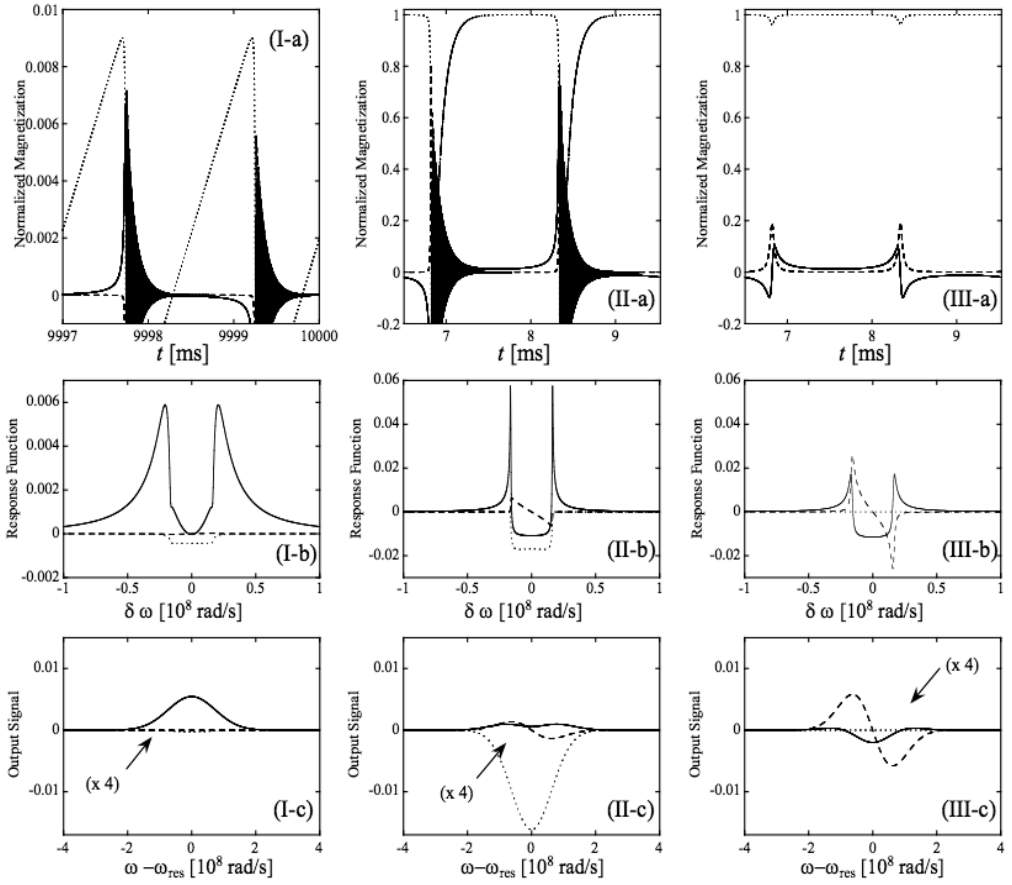

Fig. 5 Numerical calculation of Bloch equation for the inhomogeneously-broaden spectrum h (ω, ω_a). The column I is the case for $T_1 = 10^{-1}$ s and $T_2 = 10^{-4}$ s, the column II for $T_1 = 10^{-4}$ s and $T_2 = 10^{-4}$ s and the column III for $T_1 = T_2 = 10^{-6}$ s. In the raw (a), $M_x(t)$ is shown by solid line, $M_y(t)$ by dashed line and $M_z(t)$ by dotted line. In (b), $\overline{M_x \cos\omega_m t}$ is shown by solid line, $\overline{M_x \sin\omega_m t}$ by dotted line and $\overline{M_y \cos\omega_m t}$ by dashed line. In (c), $M_x^{IN}(\delta\omega)$ is shown by solid line, $M_x^{OUT}(\delta\omega)$ by dotted line and $M_y^{IN}(\delta\omega)$ by dashed line. $M_y^{IN}(\delta\omega)$ is multiplied by a factor 4.

(II-b), and (III-b) show the response functions to Bloch equations, $\overline{M_x \cos\omega_m t(\delta\omega)}$ by solid lines, $\overline{M_x \sin\omega_m t(\delta\omega)}$ by dotted lines and $\overline{M_y \cos\omega_m t(\delta\omega)}$ by dashed lines. It should be noted that in all cases, $\overline{M_x \cos\omega_m t(\delta\omega)}$ and $\overline{M_x \sin\omega_m t(\delta\omega)}$ are even functions for $\delta\omega$ and $\overline{M_y \cos\omega_m t(\delta\omega)}$ is odd function for $\delta\omega$. $\overline{M_y \sin\omega_m t(\delta\omega)}$ is negligibly small in all T_1 range and is not shown in the figure. In region I and II, $\overline{M_y \cos\omega_m t(\delta\omega)}$ is small. In region III, $\overline{M_y \cos\omega_m t(\delta\omega)}$ is the main signal and $\overline{M_x \cos\omega_m t(\delta\omega)}$ is not negligible but $\overline{M_x \sin\omega_m t(\delta\omega)}$ is much smaller than the others, because $\boldsymbol{M}$ responds to the field modulation without a delay in the slow passage region. Figures (I-c), (II-b) and (III-c) show the output signal of $M_x^{IN}(\delta\omega)$ by a solid line, $M_y^{IN}(\delta\omega)$ by a dashed line and $M_x^{OUT}(\delta\omega)$ by a dotted line. It should be noted that both $M_x^{IN}(\delta\omega)$ and $M_x^{OUT}(\delta\omega)$ are even functions for $\delta\omega$ and $M_y^{IN}(\delta\omega)$ is a odd function for $\delta\omega$. Therefore the output $V^{IN}(\delta\omega)$ calculated by Eq. (5) are almost odd function for $\delta\omega$ in III, the mixture of both even and odd function in II and purely even function in I. On the other hand, $V^{OUT}(\delta\omega)$ is always even function.

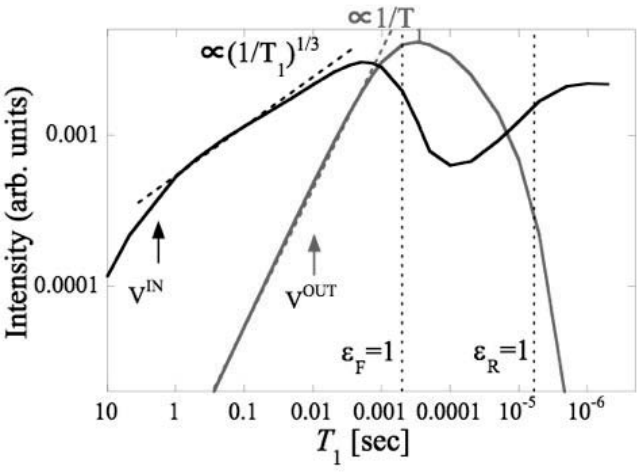

Fig. 6 Intensities of V^{IN} and V^{OUT} as a function of T_1. The mixing parameter A=4 is used to calculate $M^{IN} = M_x^{IN} + 4\,M_y^{IN}$

Once we get $V^{IN}(\delta\omega)$ and $V^{OUT}(\delta\omega)$, it is straight forward to calculate the normalized intensities by using Eq. (7). In the regions II and III, the peak-to peak values are taken for V^{IN} and the peak value for V^{IN} in the region I and for V^{OUT} in the region I and II. In Fig. 6, V^{IN} and V^{OUT} are plotted as a function of T_1. The passage parameters $\varepsilon_R = 1$ and $\varepsilon_F = 1$ are indicated by the vertical dotted-lines in the figure.

In the region I (low temperature limit), the V^{OUT} decreases proportionally to $1/T_1$ and the signal intensity mainly comes from the adiabatic rapid passage signal around $b_z(t) \sim 0$. The V^{IN} comes from the spin-locking signal ($M_x(t) \sim B_1 M_z(t) / b_z(t)$ for $\delta\omega > B_m$, where $M_z(t) \sim 1$). Therefore, $V^{OUT} >> V^{IN}$ for $\varepsilon_F >> 1$. Since the research has been focused on spin dynamics at low temperature, we will derive physical picture of the spin motion and an analytic solution for $\varepsilon_R >> \varepsilon_F >> 1$. The T_1-dependence on V^{IN} is rather complicated, as is shown in the next section.

4. Spin dynamics and analytic solution of Bloch equations for $\varepsilon_F >> 1$ in the low-temperature limit

Why is V^{IN} so much larger than V_{OUT} and both V^{IN} and V^{OUT} have different T_1-dependences for the case of $\varepsilon_F >> 1$ at low temperature? As you can see in Fig. 6, V^{IN} is proportional to $(1/T_1)^{1/3}$ in some range and V^{OUT} is proportional to $1/T_1$. Therefore, V^{IN} is very much larger than V^{OUT} at low temperatures. The T_1-dependences implies that V^{IN} are raised by the different origin from

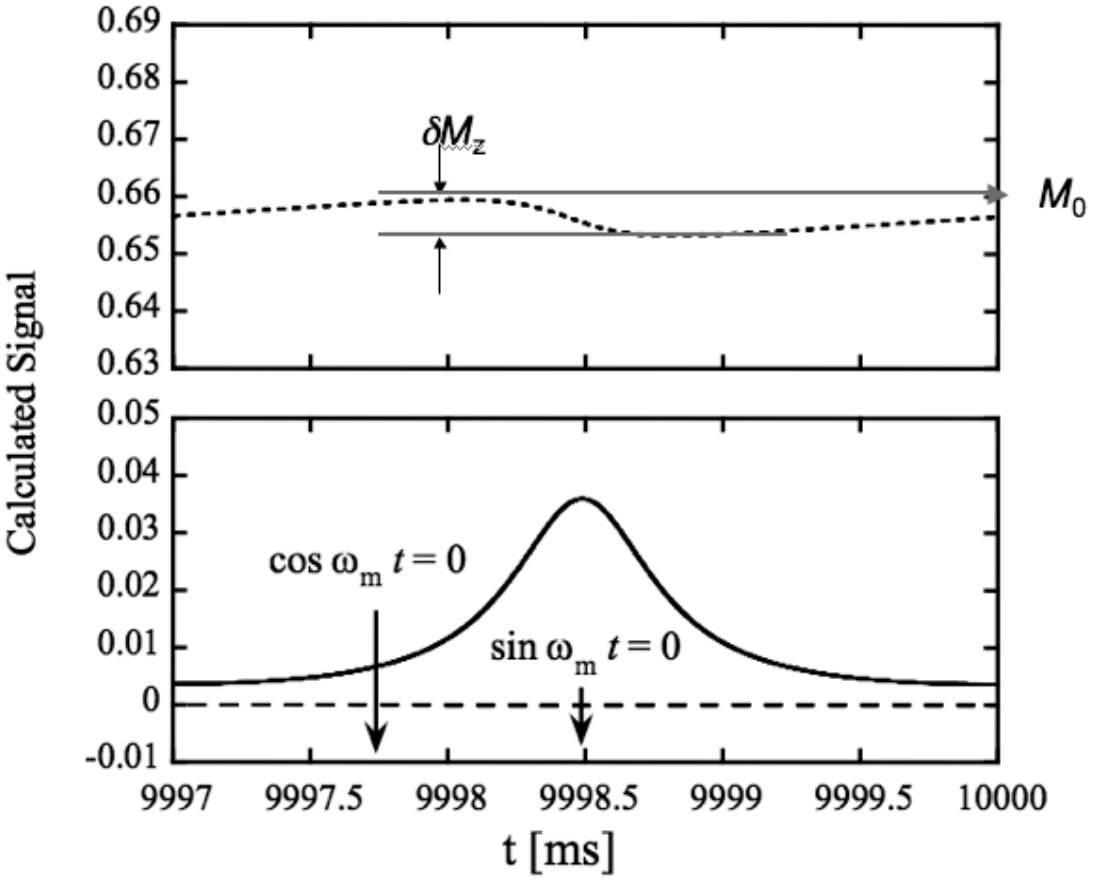

Fig. 7 $M_\alpha(t)$ for the case of $T_1 = 0.1$ sec $\varepsilon_F >> 1$ and $\delta\omega > B_m$. The upper graph shows $M_z(t)$ and the lower one shows $M_x(t)$. The point shown by sin $\omega_m t = 0$ corresponds to the time when $b_z(t)$ is the closest to the resonance but still $b_z(t) > 0$.

V^{OUT}.

See Fig. 5- Column I for the case of $T_1 = 0.1$ sec and $\varepsilon_F >> 1$. Fig. 5 (I-a) shows $M_\alpha(t)$ at $\delta\omega = 0$. It is noted that $M_z(t)$ is very small in the region where $-B_m < \delta\omega < +B_m$ because of the strong saturation effect in this region (see $M_z(t)$ in Fig. 5 (I-a), shown by a dotted line). In Fig. 5 (I-b) it should be noted that $\overline{M_x(t)sin\omega_m t}$ has a finite value within $-B_m < \delta\omega < B_m$, otherwise is almost zero. But $\overline{M_x(t)\cos\omega_m t}$ has a large value in the region that $\delta\omega < -B_m$ and $\delta\omega > +B_m$. Particularly $\overline{M_x(t)\cos\omega_m t}$ is zero at $\delta\omega = 0$.

Next, Fig. 7 shows $M_x(t)$ in the case that $\delta\omega$ ($\delta\omega = 2\text{x}10^7$ rad/s) is slightly bigger than B_m for the case of $T_1 = 0.1$ sec. Therefore, $b_z(t) = \delta\omega/\gamma + B_m \cos\omega_m t > 0$ and never goes through zero (the resonance point). In this case, $M_z(t) \sim 1$ (actually between 0.65~0.66) and $M_x(t)$ is given by,

$$M_x(t) \sim \frac{B_1}{b_z} M_z = \frac{B_1 M_z}{\delta\omega/\gamma + B_m \cos\omega_m t}, \qquad (8)$$

It should be noted that there is no adiabatic rapid passage signal appeared in Fig. 2 (thus no ringing signals) and also $M_z(t)$ is not saturated much and almost constant in time. It is very much different from $M_x(t)$ for the case that $-B_m < \delta\omega < B_m$. This signal (Eq. (8)) gives the main contribution to $\overline{M_x(t)\cos\omega_m t}$.

On the other hand, $\overline{M_x(t)sin\omega_m t}$ signal comes from the quasi-adiabatic rapid passage signal at resonance and then becomes progressively small when $M_z(t)$ becomes saturated. I believe that

V^{OUT} is treated by Chiba and also Weger but nobody has not discussed about V^{IN} for $\varepsilon_F >> 1$ yet. In the case of $\varepsilon_F >> 1$ and $b_z(t) = \delta\omega/\gamma + B_m \cos\omega_m t > 0$, the quasi-stationary solutions of Bloch equations for $M_x(t)$, $M_y(t)$ and $M_z(t)$ are obtained by taking $dM_x/dt = dM_y/dt = dM_z/dt = 0$

$$M_y(t) = -\frac{B_1}{\gamma b_z T_2} M_x(t) << M_x(t) \tag{9}$$

The $M_x(t)$ is given by Eq. (8), neglecting $M_y(t)$-term and $M_z(t)$ is given by,

$$\left(1 + \frac{T_1}{T_2}\left(\frac{B_1}{b_z(t)}\right)^2\right) M_z(t) = 1 \tag{10}$$

Taking the time average for Eq. (10), approximating that $M_z(t)$ is almost constant over the period of the time and being replaced by M_0 ($\overline{M_z(t)} = M_0$), we obtain,

$$\left(1 + \frac{T_1}{T_2}\overline{\left(\frac{B_1}{b_z(t)}\right)^2}\right) M_0 = 1$$

$$M_o = \frac{1}{1 + \left(\frac{T_1}{T_2}\right)\left(\frac{B_1}{B_m}\right)^2 \frac{(\delta\omega/\gamma B_m)}{((\delta\omega/\gamma B_m)^2 - 1)^{3/2}}} \tag{11}$$

Let us calculate $M_x(t)$ in the limit of $\varepsilon_F >> 1$. We define $\cos\alpha_0$ as,

$$\cos\alpha_0 = \frac{\delta\omega - \gamma B_m}{\sqrt{(\delta\omega - \gamma B_m)^2 + \gamma^2 B_1{}^2}} \tag{12}$$

Using Eq. (8) and $M_z \sim M_0$, $M_x(t)$ is approximately given by,

$$\begin{aligned} M_x(t) &= M_0 \sin\alpha(t) = M_0 \alpha(t) \\ &= M_0 \frac{B_1}{\delta\omega - B_m \cos\omega_m t} \\ &= \frac{1}{1 + \left(\frac{T_1}{T_2}\right)\left(\frac{B_1}{B_m}\right)^2 \frac{(\delta\omega/\gamma B_m)}{((\delta\omega/\gamma B_m)^2 - 1)^{3/2}}} \frac{\gamma B_1}{(\delta\omega - \gamma B_m \cos\omega_m t)} \end{aligned} \tag{13}$$

It is clear that M_x has only the in-phase signal and $\overline{M_x \sin\omega_m t} = 0$. Inserting Eq. (13) into Eq. (5), we obtain,

$$\overline{M_x \cos\omega_m t} = \frac{1}{1 + \left(\frac{T_1}{T_2}\right)\left(\frac{B_1}{B_m}\right)^2 \frac{(\delta\omega/\gamma B_m)}{((\delta\omega/\gamma B_m)^2 - 1)^{3/2}}} \frac{B_1}{B_m}\left[\frac{\delta\omega}{\sqrt{(\delta\omega)^2 - \gamma^2 B_m^2}} - 1\right] \tag{14}$$

$$\overline{M_x \sin\omega_m t} = 0 \tag{15}$$

These solutions should be compared with Fig. 8 attached below in this section. Dotted blue points are calculated by Eq. (14) and should be compared with the red curve calculated by numerical solution in the range where $|\delta\omega - \gamma B_m| > 0$. Those agree very well with each other and Eq. (14) is the analytic solution of spectrum function for Bloch equation in the case that $\varepsilon_R >> \varepsilon_F >>1$. It should be mentioned that if we can measure ESR for enriched ^{28}Si:P samples and ESR line width is determined by the homogeneous broadening, then two signals which are separated at $\delta\omega = \pm\gamma B_m$ appears and no signal at resonance for $\varepsilon_F >> 1$.

It is clear that the above signal appears purely in the in-phase signal of M_x. On the other hand, the adiabatic rapid passage signal appears both in the in-phase and the out-of-phase of M_x. However, the rapid passage signal is quickly saturated and disappears for the case of $\varepsilon_F >>1$.

We still have to take a convolution of Eq. (6) with h (ω, ω_a) and calculated the peak values of the spectrum to get the final answer for V^{IN}.

$$M_x{}^{IN}(\omega) = \int_{-\infty}^{\infty} \overline{M_x \cos\omega_m t\,(\omega - \omega')}\, h(\omega', \omega_a)\, d\omega' \tag{16}$$

Since Eq. (14) agrees with the numerical solution, Eq. (16) will reproduce the results for V^{IN} for $\varepsilon_F >>1$ and $T_1 < 0.1$ sec, shown in Fig. 6. Between 0.1 sec > T_1 > 0.01 sec, V^{IN} contains the same size as V^{OUT}(the rapid passage signal), which is about 10 % of the total V^{IN}.

When $\gamma B_1 << \sigma$, then h (ω, ω') can be regarded to be slowly-varying function of $\delta\omega$, and be taken out from integral, Eq. (16) can be calculated as,

$$M_x{}^{IN}(\omega) = h(\omega, \omega_a) \int_{-\infty}^{\infty} \overline{M_x \cos\omega_m t\,(\omega - \omega')}\, d\omega' \tag{17}$$

However, main contribution for the integral comes from large values of $\delta\omega$, we have to use the cut-off for $\delta\omega$. Inserting Eq. (14) into Eq. (17) with the cot-off at δω = σ, we obtained,

$$\begin{aligned}\int_{-\infty}^{\infty} M_x(\omega - \omega')\, d\omega' &= 2\int_{\gamma B_m}^{\sigma} d(\delta\omega) \frac{1}{1 + \left(\frac{T_1}{T_2}\right)\left(\frac{B_1}{B_m}\right)^2 \frac{(\delta\omega/\gamma B_m)}{((\delta\omega/\gamma B_m)^2 - 1)^{3/2}}} \frac{B_1}{B_m}\left[\frac{\delta\omega}{\sqrt{(\delta\omega)^2 - \gamma^2 B_m^2}} - 1\right] \\ &= 2\int_1^{\sigma/\gamma B_m} \gamma B_m\, dx \frac{1}{1 + \left(\frac{T_1}{T_2}\right)\left(\frac{B_1}{B_m}\right)^2 \frac{x}{(x^2-1)^{3/2}}} \frac{B_1}{B_m}\left[\frac{x}{\sqrt{x^2 - 1}} - 1\right]\end{aligned} \tag{18}$$

where we introduce $x = \delta\omega/\gamma B_m\,(x: 1 \to \sigma/\gamma B_m)$.

The final in-phase signal V^{IN} is given by,

$$V^{IN} = M^{IN}(\omega = \omega_a) = \frac{2\gamma B_1}{\sqrt{2\pi}\sigma} \int_1^{\sigma/\gamma B_m} dx \frac{1}{1 + \left(\frac{T_1}{T_2}\right)\left(\frac{B_1}{B_m}\right)^2 \frac{x}{(x^2-1)^{3/2}}} \left[\frac{x}{\sqrt{x^2 - 1}} - 1\right] \tag{19}$$

We can reproduce V^{IN} very well for $T_1 > 0.01$ sec by Eq. (19). As mentioned before, for $T_1 <$ 0.01 sec and $\varepsilon_F > 1$, there is a small fraction of the rapid-passage signal in V^{IN}, which is the same order of magnitude as V^{OUT} in this range (see the red and blue curves in Fig. 8 in the range where $\delta\omega < \gamma B_m$).

Figures attached below are the same as Fig. 5. Fig. I-a ($\delta\omega = 0$) should be compared with Fig. 7 ($\delta\omega = 2 \times 10^7$ rad/s).

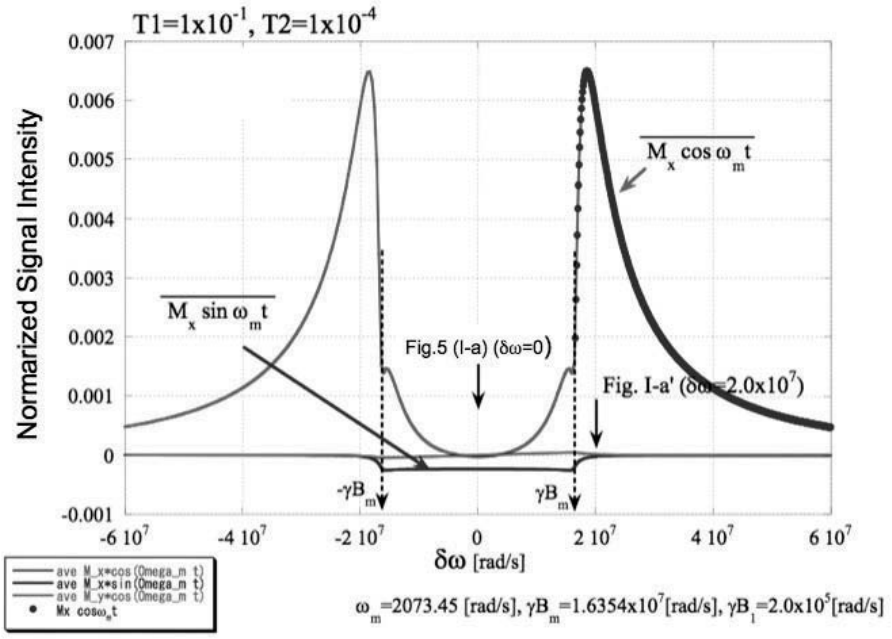

Fig. 8 This graph is the same as Fig. 5 (I-b) but more details are shown. Blue dotted points are calculated values of $\overline{M_x(t)\cos\omega_m t}$ by Eq. (14).

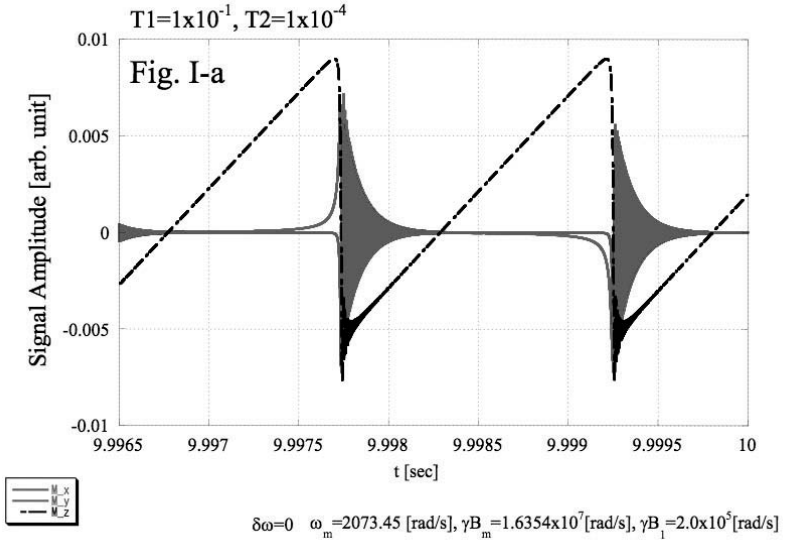

The above graph is the same as Fig. 5 (I-a) but is shown in a larger scale.

5. Temperature dependence of T_1 at a high field of 3 T.

"Intensities vs. T_1" derived by numerical simulation of Bloch equation (Fig. 6) should be compared with the experimental result of "intensities vs. T "(Fig. 3) . The T_1 vs. T are shown in Fig. 8, where squares are T_1 derived from V^{IN} and circles are T_1 from V^{OUT}. It should be noted here that the fitting parameter B_1 in this analysis are determined in such a way that $T_1(T)$ derived at $\varepsilon_R = 1$ (shown by the arrow with "B_1 fixed") are forced to be on the heavy solid line.

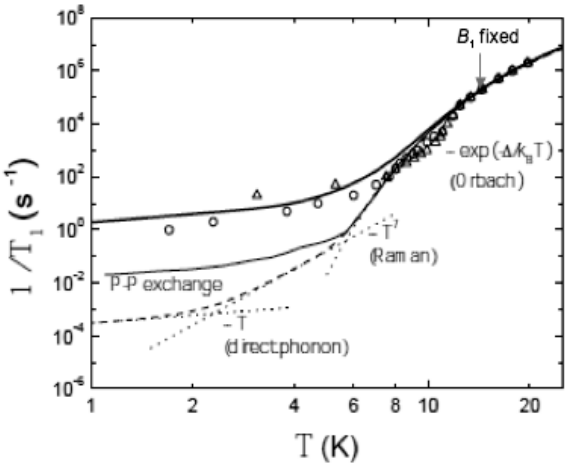

Fig. 8 Temperature dependence of T_1 at B = 3 T. The dashed line indicates T_1 at B = 0.3 T for $n < 10^{16}$cm^{-3} [6, 7, 12] and the thin solid line is T_1 for n = 7 x 10^{16} cm^{-3} at B = 0.3 ~ 0.8 T [6]. Triangles are derived from V^{IN} and circles are from V^{OUT}.

The dashed line indicates T_1 values at B = 0.32 - 0.33 T for $n < 10^{16}$cm^{-3} [6, 7, 12], below which T_1 is independent of P-concentration but depends strongly on T and B. The T_1 (T, H) is given by [7],

$$\frac{1}{T_1} = 2.9\times10^{-2} B^4 T + 2.0\times10^{-5} B^2 T^7 + 0.91\times10^{9} \exp\left(\frac{\Delta}{k_B T}\right), \qquad (20)$$

where B in T, T in K and $\Delta / k_B T$ = 122.5 K. The T_1 value scaled at B = 2.87 T is shown by the heavy solid line. The 1st term corresponds to the phonon direct process, the 2nd one to Raman process and the 3rd one to Orbach process [23], which does not depend on B.

The T_1 for n > 1 x 10^{16} cm^{-3} depends on n. The thin solid line is T_1 for n = 7 x 10^{16} cm^{-3} at B = 0.3 ~ 0.8 T [6]. The concentration is similar to our sample. The T_1 mechanism are attributed to the exchange coupling between neighboring P-donors [24] and should be field-independent. Because of strong field-dependance of the phonon direct process (proportional to B^4), the impurity-dependent exchange relaxation should be masked by the direct process at B = 2.87 T at low temperatures. Our measured values of T_1 (T) agree very well to the heavy solid line.

It is interesting to extrapolate the measured value of T_1 at B = 3 T and T = 1 K to T = 100 mK. The expected T_1 at 100 mK and 3 T is about 10 s and can be even shorter for higher fields, which make it possible to cool the isolated electron spin temperature down to 100 mK.

6. Dynamic Nuclear Polarization of P-Nuclear Spins

The DNP in Si:P has been studied at $B = 0.32$ T by Feher [14]. Also the DNP has been discussed from the shift of the cluster of P impurities [16]. Recently the DNP effect has been reported by irradiation of visible light [17]. Similar DNP result as our results at a high field of 8 T was recently reported [25].

Figure 3 shows that H-line (open symbols) is a little bit smaller than L-line (solid symbols) at low temperatures. This asymmetry between two lines becomes significant below about 10 K. Present ESR data were taken by sweeping magnetic field back and forth between two lines every 30 minutes under continuous radiation of the microwave. The asymmetry between H- and L-line suggests that the DNP may occur on P-nuclear spins. In order to confirm the DNP, the resonance signal was observed just after cooling from 77 K down to 6.9 K. The result is shown in Fig. 9 (a). The in-phase signal is shown by thick line and the out-of-phase signal by thin line. Both in-phase and out-of-phase signals shows that the intensities of the H- and L- lines are almost equal. Next, the microwave was irradiated at the H-line for 20 minutes. The observed ESR spectrum is show in Fig. 9 (b). The intensity of L-line is about 10 % higher than that of H-line both for in-phase and out-of-phase signals. We believe that this asymmetry are attributed to the DNP of P-nuclear spins and the nuclear polarization is enhanced by 1000 times over the thermal equilibrium values of P-nuclear polarization at $T = 6.9$ K.

It is very important to extend the DNP to lower temperatures and confirm the full polarization of the P-nuclear spins. It is most desired to investigate directly NMR of P-nuclei and study spin dynamics at high fields of several T and low temperatures of 100 mK by using the DNP.

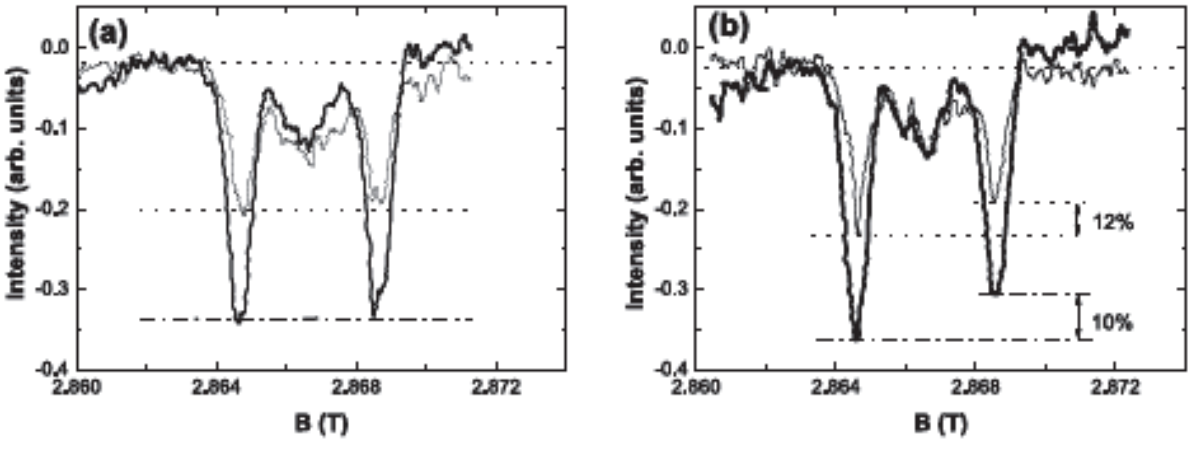

Fig. 9. The DNP of P-nuclei by pumping the H-line for 20 minutes. (a) Spectra taken right after cooling from 77 K to 6.9 K. (b) Spectra taken after irradiation of the microwave.

7. Summary

cw-ESR for insulator sample of Si:P ($n = 6.5 \times 10^{16}$cm^{-3}) has been investigated at 80 GHz at $B \sim 3$ T in the temperature range between 50 K and 1.5 K. The spectra shape changes as temperatures are lowered. We solve Bloch equation numerically as a function of $T_1(T)$ and explain the change in spectrum by change of the various passage conditions. Numerical analysis and physical picture of the spin dynamics for $\varepsilon_F >> 1$ at low temperatures are discussed in detail. Comparing temperature-dependence of intensities between experiment and numerical solution of Bloch equations, $T_1(T)$ are for the first time derived at $B = 2.87$ T. The T_1 at low temperatures is determined by the phonon direct process. We extrapolate the measured T_1 at 3 T and 1 K down to 100 mK and the estimated T_1 at 100 mK is about 10 s. This values of T_1 is manageable to cool down the electron spin temperature down to 100 mK. We found that the DNP was very effective at high fields of 3 T and achieved 1000 times enhancement in P-nuclear spins polarization over the thermal equilibrium value. The DNP can be used to set up the initial condition of Q-bits. Direct observation of NMR to investigate spin dynamics of P-nuclear spins are future project for application of the DNP.

Acknowledgment

Through the Japan-Korea Joint Project, Fukui and Kyoto University in Japan and KAIST in Korea have been working to study basic sciences and material properties of Si:P system and report on problems 1) and 2) by using high frequency ESR (80 GHz) at 3 T.

References

[1] B. E. Kane, Nature **393** 133 (1998)
[2] M. Jeong , M. Song, T. Ueno, T. Mizusaki, A. Matsubara, and S. Lee, J. Phys. Soc. Jpn. **78**, 075003 (2009).
[3] M. Jeong, M. Song, T. Ueno, T. Mizusaki, A. Matsubara and S. Lee, J. Low Temp. Phys. **158**, 659 (2010)
[4] M. Song M, M. Jeong, T. Ueno, B. Kang, K. Sugiyama, K. Tanaka, A. Matsubara, S. Lee, S. Mitsudo, T. Mizusaki, and M. Chiba, J. Phys.: Conf. Ser. **150**, 022078 (2009)
[5] M. Song, M. Jeong, B. Kang, S. Lee, T. Ueno, A. Matsubara, T. Mizusaki, Y. Fujii, S. Mitsudo and M. Chiba, J. Phys.: Condensed matter **22**, 206001 (2010)
[6] G. Feher and E. A. Gere, Phys. Rev. **114**, 1245 (1959)
[7] T. G. Castner Jr., Phys. Rev. **130**, 58 (1963)
[8] R. C. Fletcher, W. A. Yager, G. L. Pearson , A. L. Hilden, W. T. Read, and F. R. Merritt, Phys. Rev. **94**, 1392 (1954)
[9] S. Maekawa and N. Kinoshita J. Phys. Soc. Jpn. **20**, 1447 (1965)
[10] G. Feher, Phys. Rev. **114**, 1219 (1959)
[11] M. Chiba and A. Hirai, J. Phys. Soc. Jpn **33**, 730 (1972)
[12] A. M. Tyryshkin, A. A. Lyon, A. V. Astashkin, and A. M. Raitsimring, Phys. Rev. B **68**, 193207 (2003)
[13] T. G. Castner Jr., Phys. Rev. Lett. **8** 13 (1962)
[14] G. Feher, Phys. Rev. **103**, 500 (1956).
[15] G. Feher and E. A. Gere, Phys. Rev. **103**, 501(1956).
[16] K. Morigaki and M. Rosso, J. Physique **36**, 1131 (1975)

[17] D. R. McCamey, J. van Tol, G. W. Morley, and C. Boehme, Phys. Rev. Lett. **102**, 027601 (2009)
[18] G. W. Morley, D. R. McCamey, H. A. Seipel, L/ C. Brunel, J. van Tol, and C. Boehme, Phys. Rev. Lett. **101**, 027602 (2009)
[19] T. F. Rosenbum et al., Phys. Rev. **B27**, 7509 (1983)
[20] A. Abragam, *Principles of Nuclear Magnetism, Chap. X Sec. IV* (New York: Oxford University Press, 1961)
[21] A. M. Portis, Phys. Rev. **100**, 1219 (1956).
[22] M. Weger, Bell Syst. Tech. J. **34**, 1013 (1960).
[23] R. Orbach, *Proc. Phys. Soc. London* **77** 821 (1961)
[24] D. Pines, J. Bardeen, and C. P. Slichter, Phys. Rev. **106**, 489 (1957)
[25] J. van Tol et al., Appl. Magnetic Reson. **36**, 259 (2009)